JACS
JOURNAL OF THE AMERICAN CHEMICAL SOCIETY

Article

pubs.acs.org/JACS

Unraveling the Mechanism of Catalytic Reduction of O_2 by Microperoxidase-11 Adsorbed within a Transparent 3D-Nanoporous ITO Film

Christophe Renault,[†] Claude P. Andrieux,[†] Ryan T. Tucker,[‡] Michael J. Brett,[‡,§] Véronique Balland,*[,†] and Benoît Limoges*[,†]

[†]Laboratoire d'Electrochimie Moléculaire, UMR CNRS 7591, Université Paris Diderot, Sorbonne Paris Cité, 15 rue Jean-Antoine de Baïf, F-75205 Paris Cedex 13, France

[‡]Electrical and Computer Engineering, University of Alberta, Edmonton, Alberta, Canada T6G 2V4

[§]NRC National Institute for Nanotechnology, Edmonton, Alberta, Canada T6G 2M9

Supporting Information

ABSTRACT: Nanoporous films of indium tin oxide (ITO), with thicknesses ranging from 250 nm to 2 μm, were prepared by Glancing Angle Deposition (GLAD) and used as highly sensitive transparent 3D-electrodes for quantitatively interrogating, by time-resolved spectroelectrochemistry, the reactivity of microperoxidase-11 (MP-11) adsorbed within such films. The capacitive current densities of these 3D-electrodes as well as the amount of adsorbed MP-11 were shown to be linearly correlated to the GLAD ITO film thickness, indicating a homogeneous distribution of MP-11 across the film as well as homogeneous film porosity. Under saturating adsorption conditions, MP-11 film concentration as high as 60 mM was reached. This is equivalent to a stack of 110 monolayers of MP-11 per micrometer film thickness. This high MP-11 film loading combined with the excellent ITO film conductivity has allowed the simultaneous characterization of the heterogeneous one-electron transfer dynamics of the MP-11 Fe^{III}/Fe^{II} redox couple by cyclic voltammetry and cyclic voltabsorptometry, up to a scan rate of few volts per second with a satisfactory single-scan signal-to-noise ratio. The potency of the method to unravel complex redox coupled chemical reactions was also demonstrated with the catalytic reduction of oxygen by MP-11. In the presence of O_2, cross-correlation of electrochemical and spectroscopic data has allowed us to determine the key kinetics and thermodynamics parameters of the redox catalysis that otherwise could not be easily extracted using conventional protein film voltammetry. On the basis of numerical simulations of cyclic voltammograms and voltabsorptograms and within the framework of different plausible catalytic reaction schemes including appropriate approximations, it was shown possible to discriminate between different possible catalytic pathways and to identify the relevant catalytic cycle. In addition, from the best fits of simulations to the experimental voltammograms and voltabsorptograms, the partition coefficient of O_2 for the ITO film as well as the values of two kinetic rate constants could be extracted. It was finally concluded that the catalytic reduction of O_2 by MP-11 adsorbed within nanoporous ITO films occurs via a 2-electron mechanism with the formation of an intermediate Fe^{III}–OOH adduct characterized by a decay rate of 11 s^{-1}. The spectroelectroanalytical strategy presented here opens new opportunities for characterizing complex redox-coupled chemical reactions not only with redox proteins, but also with redox biomimetic systems and catalysts. It might also be of great interest for the development and optimization of new spectroelectrochemical sensors and biosensors, or eventually new photoelectrocatalytic systems or biofuel cells.

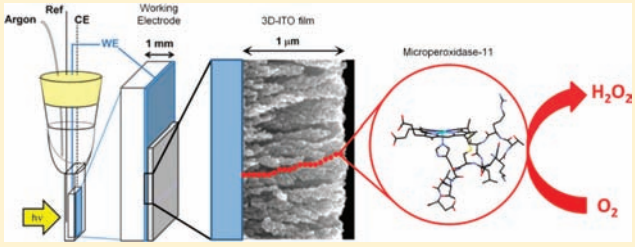

INTRODUCTION

Electrochemical characterization of redox-active proteins or enzymes immobilized on a conductive substrate is a powerful strategy for analyzing the thermodynamic and kinetic processes of biological electron transfer and for revealing the link to biologically important coupled chemical reactions. It is also of great interest for the development of biotechnological applications such as biosensors, biofuel cells, or bioreactors.[1−5] A key advantage resulting from the immobilization of proteins on an electrode surface is that it shortens the distance between the redox-active protein and the electrode, hence, facilitating the electron transport/transfer communication with the active site. Another advantage is the very small quantities of material required for an experiment. During the past decade, the possibility to address the intricate chemistry of immobilized redox enzymes or proteins by direct electron transfer between their individual redox-active sites and the electrode has been shown to be particularly useful for accessing mechanistic and kinetics data.[6,7] In parallel, substantial progress has been made

Received: February 6, 2012
Published: March 26, 2012

   dx.doi.org/10.1021/ja301193s | *J. Am. Chem. Soc.* 2012, 134, 6834−6845

in the development of theoretical tools for analyzing under direct or mediated electron transfer the mechanisms and kinetics of redox enzymes immobilized on an electrode surface.[7−9] The main strength of direct compared with mediated electron transfer lies in the high degree of control over the redox status of immobilized protein through the electrode potential, thus, offering a continuous spectrum of driving forces for characterizing complex redox-coupled chemical reactions. Moreover, experiments may be carried out over a wide range of accessible time scales to view both transient and steady-state processes occurring in the same sample. However, a frequently encountered problem is that the electroactive coverage of redox-active proteins is often too low to produce detectable signals from direct oxidation or reduction of their redox centers.[7] Consequently, most of the electrochemical studies dealing with direct electrochemistry of redox enzymes were achieved in the presence of their substrate to take advantage of the catalytic amplification of the current signal. However, the absence of precise knowledge of the electroactive enzyme coverage remains an important drawback for quantitative analysis of catalysis. Another limitation of direct protein-film electrochemistry is that the measured current is an indirect observable of the electron transfer reaction as well as of the coupled chemical reactions, with the consequence that no information is available on the chemical nature of events associated with the electron transfer. It fails therefore in attributing unambiguously the redox potentials and in identifying the chemical nature of transient intermediates. It fails also in answering the essential question of whether proteins retain their native structure or not in the adsorbed state. The measured current may also be affected by charging current related to the electrode double layer capacitance, as well as by faradaic current associated with other redox species present in the electrolyte or adsorbed to the electrode surface, therefore, complicating the unambiguous observation of redox protein-film chemistry.

The coupling of protein-film electrochemistry with a time-resolved spectroscopy is an attractive way to overcome some of the drawbacks mentioned above.[10,11] An immediate advantage of monitoring an optical instead of a current signal upon electrode polarization is its freedom from nonfaradic contribution (i.e., no capacitive current as in cyclic voltammetry or chronoamperometry),[12] leading thus to a much cleaner signal. Another benefit is the higher selectivity offered by a spectroscopic signal, allowing, for example, multicomponent analysis during a single potential step (or sweep) by appropriately monitoring a selection of wavelengths.[13] Very few methods combining protein-film electrochemistry and time-resolved spectroscopy have been proposed so far. Among them, surface-enhanced resonance Raman spectroscopy[14] and surface enhanced infrared absorption[15] coupled to chronoamperometry were shown efficient for probing the molecular structure and interfacial electron-transfer dynamics of hemoproteins assembled on metallic electrodes. These techniques are however mostly restricted to proteins containing heme groups and they also require rather sophisticated and costly instrumentations. Spectroelectrochemical characterization of redox proteins immobilized in transparent semiconductive mesoporous metal oxide films appear as a more versatile and simpler alternative strategy.[12,13] This is especially true if a sufficiently short time resolution can be achieved.[10] Thanks to their high specific surface area, the mesoporous metal oxide electrodes enable the immobilization of a large number of proteins (equivalent to several tens of packed monolayers) which can in turn be properly detected by spectroscopic techniques such as UV−visible absorption spectroscopy. Moreover, because of their semiconductive properties, adsorbed redox proteins can undergo redox conversion upon electrode polarization by direct interfacial electron transfer. This was demonstrated for a range of small redox proteins adsorbed in porous films of randomly sintered nanoparticles of TiO_2 or SnO_2.[12,13,16,17] However, a major shortcoming with these films is their semiconductive properties which restrict their use as a metal-like electrode to potential lower than −0.4 V for TiO_2 and +0.2 V for SnO_2 (vs ECS). For more positive potentials, the electrode Fermi levels lie within the semiconductor bandgap and the film is therefore insulating. To overcome such a limitation, we have recently proposed to take advantage of optically transparent conductive films of nanoporous ITO prepared by vacuum-based glancing angle deposition (GLAD).[18] These metal-like conductive films are typically made of nanosized columnar structures with a relatively well-defined nanoporosity and controlled film thickness. Moreover, as a result of their high specific surface area and conductivity over a wide potential window, they were shown as a practical platform for the immobilization of a small redox protein such as microperoxidase-11 (MP-11) and for the monitoring of the transient redox heme conversion (i.e., Fe^{III}/Fe^{II} couple) by the combined used of cyclic voltammetry and cyclic voltabsorptometry up to a time resolution of few tens of milliseconds.[18]

In the present paper, we explore in more detail the potential offered by nanoporous 3D-transparent GLAD ITO electrodes for time-resolved spectroelectrochemistry of MP-11. In particular, the influence of the GLAD ITO film thickness on the spectroelectrochemical detection of MP-11 is examined and the ability to quantitatively and dynamically characterize the different redox states of MP-11 by cyclic voltammetry and cyclic voltabsorptometry is carefully investigated. The potency of the method to unravel complex redox-coupled chemical reactions is also demonstrated with the catalytic reduction of oxygen by MP-11. Notably, it will be shown how it may be possible, on the basis of numerical simulations of cyclic voltammograms and voltabsorptograms and within the framework of different plausible catalytic reactions schemes, to discriminate between a 2- and a 4-electron catalytic reaction scheme.

RESULTS AND DISCUSSION

GLAD ITO Electrodes. The nanoporous films of ITO were prepared under vacuum by glancing angle deposition of ITO pellets, followed by thermal treatment. The main advantage of this technique is that it allows the production of highly porous films made of nanosized columnar structures of ITO with easily adjustable thickness, porosity, surface area, and shape.[19,20] A deposition angle of $\alpha = 80°$ was selected because this is a good compromise between a well opened porosity (∼0.5) and a high surface area enhancement (∼75 μm^{-1}).[21] In Figure 1 are shown the cross-sectional and top-view SEM images of GLAD ITO films having four different film thicknesses l (ranging from 0.25 to 2 μm). It can be clearly discerned from the images that, as the film thickness is increased, the density of nanocolumns is decreased (from ca. 70 to 8 columns per μm^2) as their diameter is increased (from ∼90 to 270 nm). Moreover, the void spacing between the nanocolumns concurrently increases (from ∼40 to 90 nm). The optical transparency of the ITO films was

dx.doi.org/10.1021/ja301193s | J. Am. Chem. Soc. 2012, 134, 6834−6845

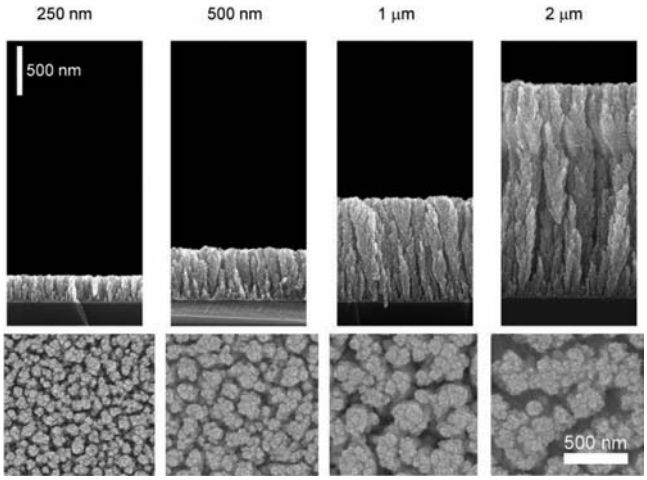

Figure 1. SEM images (side- and top-views) of GLAD ITO films prepared with a deposition angle of 80° and for different film thicknesses.

characterized by UV−visible absorption spectroscopy. Given the relatively large bandgap value of ITO, the porous films are mostly transparent in the visible part of the spectrum. However, the optical transparency is gradually affected when the film thickness increases, especially in the UV region because of the large increase of band-to-band absorbance as well as the increased optical scattering as the column features broaden with increasing thickness (Figure 2A). For suitable spectroscopic

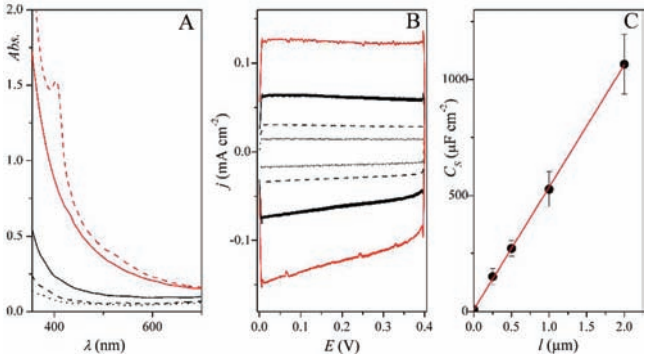

Figure 2. (A) UV−visible absorption spectra and (B) cyclic voltammograms (scan rate 0.1 V s^{-1}) of GLAD ITO films of (black dotted line) 0.25, (black hashed line) 0.5, (black solid line) 1.0, and (red solid line) 2.0 μm. In panel A is also reported the UV−visible spectrum (red hashed line) of the 2.0 μm-thick GLAD ITO film loaded with a half-saturating concentration of MP-11. (C) Change of the film capacitance density C_S (determined at 0.1 V in cyclic voltammetry and normalized to the geometric electrode area S) as a function of film thickness l (each data point is the average value resulting from at least 4 measurements obtained from 4 separate electrodes, error bars are the standard deviation). Red line: linear regression fitting given by $C_S = 530 \times l + 8$ (in μF cm^{-2}). All experiments were carried out in 75 mM Hepes + 25 mM NaCl (pH 7, T = 25 °C).

characterization of an adsorbed molecule, it is thus important to select an appropriate GLAD ITO film thickness that compromises between good film transparency (thin films) and high surface area enhancement (thick films).

The relationship between the specific surface area of GLAD ITO films and the film thickness was evaluated from the capacitive current recorded in cyclic voltammetry (Figure 2B). A well-defined linear dependence of the electrode capacitance density with the film thickness was observed (Figure 2C). This suggests a homogeneous increase of the specific surface area with the film thickness. It may seem a surprising result considering the fractal aspect of the nanostructured film on the SEM images and the progressive growth of ITO column diameters with their height (Figure 1), but it is in agreement with results obtained for GLAD TiO_2 films deposited at oblique angles from 70 to 85° and for which the specific surface area (determined using the Kr BET method) normalized to the projected film area was shown to rise linearly with film thickness.[22] Such a linear increase in surface area indicates that effects of column broadening do not significantly change the effective surface area as a function of the height of the film within the thickness range explored. From the slope of the linear regression in Figure 2C, a capacitance density enhancement of 530 μF cm^{-2} μm^{-1} is obtained. Assuming that the intrinsic capacitance of the GLAD ITO film is the same as the underlying bulk crystalline ITO electrode (i.e., 8 ± 2 μF cm^{-2}), we can thus estimate a surface area enhancement of 66 ± 13 per μm of film thickness. This value is in fairly good agreement with the one previously found during the quantitative cyclic voltammetric detection of ferrocene dicarboxylic acid adsorbed in similar GLAD ITO films (~75 μm^{-1}).[21]

Immobilization. MP-11 was adsorbed in the porous ITO films by soaking the GLAD ITO electrodes in a solution of MP-11 (i.e., 50 μM in a Hepes buffer, pH 7.0) during an adsorption time ranging from few minutes to several hours. After rinsing, the electrodes were characterized by UV−visible spectroscopy in a protein-free Hepes buffer. A typical raw spectrum is shown in Figure 2A in the case of a 2 μm-thick film and 30 min adsorption time, whereas blank subtracted spectra obtained under same conditions and for each of the four different film thicknesses are shown in Figure 3A. From the magnitude of the

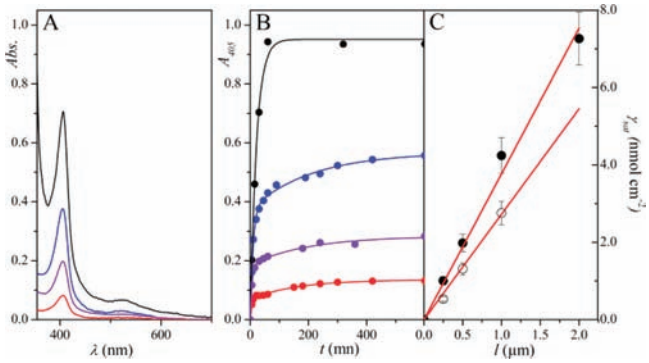

Figure 3. (A) UV−visible absorption spectra recorded at four GLAD ITO electrodes having four different film thicknesses and after 30 min adsorption in a 50 μM MP-11 solution (each spectrum was corrected from the blank spectrum of GLAD ITO electrode recorded just before MP-11 adsorption) and (B) the resulting kinetic plots of MP-11 Soret band absorbance as a function of adsorption time. The GLAD ITO film thickness is: (red) 0.25, (violet) 0.5, (blue) 1, and (black) 2 μm. All experiments were carried out at T = 20 °C in a 10 mM Hepes buffer, pH 7.0. The solid lines correspond to a double exponential fits, except for the 2 μm-thick film for which a single exponential fit was used. (C) Saturating surface concentration of adsorbed MP-11 as a function of GLAD ITO film thickness: (●) data determined from the adsorption kinetic in panel B, and (○) after the poorly adsorbed fraction of MP-11 has been desorbed.

dx.doi.org/10.1021/ja301193s | J. Am. Chem. Soc. 2012, 134, 6834−6845

Soret band (λ = 405 nm) as a function of adsorption time (t), the adsorption rate of MP-11 was determined for the four separate GLAD ITO film thicknesses (Figure 3B). For thicknesses ranging from 0.25 to 1 μm, adsorption kinetics follows a double exponential function, suggesting a fast primary adsorption process during which ~60% MP-11 adsorbs rapidly with an apparent rate constant of 0.2 ± 0.05 min^{-1} (k_{abs}), followed by a secondary slower adsorption phase with an apparent rate constant of 0.005 min^{-1}. This behavior is in line with the coexistence of two MP-11 populations in GLAD ITO films, a first one corresponding to a strongly adsorbed fraction that cannot be easily removed from the film and a second one related to a poorly adsorbed fraction that can more rapidly desorb.[18] The fraction of strongly adsorbed MP-11 depends on the film porosity. It was previously estimated to be 80% for a film porosity of 0.36 (α = 75°).[18] In the present study, wherein the film porosity is 0.48 (α = 80°), it is estimated to be almost 60%. Such a 25% decrease of the strongly adsorbed fraction of MP-11 correlates quite well with the 25% decrease of specific surface area when the deposition angle α is changed from 75 to 80°.[21] This result also suggests that the strongly adsorbed MP-11 fraction is directly adsorbed on the metal oxide surface, whereas the poorly adsorbed fraction is probably just present into the void volume of the nanoporous structure, in weak interaction with the first layer. For the 2 μm film thickness, the number of experimental records on the curve was too low for being able to discern a double exponential kinetic. Therefore, it was simply fitted to a single exponential function.

The maximal Soret band absorbance of the oxidized form of MP-11 (Fe^{III}-MP-11) in the ITO film is localized at 405 nm, which is similar to the value obtained for micromolar solutions of MP-11. This suggests that the immobilized heme remains as a hexacoordinated low-spin Fe^{III}. The nature of the sixth-ligand was assumed to be the same as in homogeneous solution (i.e., an amino residue of either the terminal lysine or of Val_{10}[23]). From the maximal values of optical density in Figure 3B, the saturated surface concentration γ_{sat} of MP-11 (i.e., in mol per unit of projected area of GLAD ITO film) was determined, assuming a Soret band extinction coefficient of $\varepsilon_{405}^{Fe^{III}} = 1.3 \times 10^5$ M^{-1} cm^{-1}.[24,25] The resulting plot of γ_{sat} as a function of film thickness shows a linear relationship (Figure 3C). From the linear regression slope associated with the films free of poorly adsorbed MP-11, a value of 2.85×10^{-9} mol cm^{-2} μm^{-1} was calculated. This value also corresponds to a volume concentration of $C^0_{f,MP\text{-}11}$ = 59 mM Fe^{III}-MP-11 (i.e., concentration in the void fraction of the porous film, considering a film porosity of 0.48). Assuming, on the basis of simple geometrical considerations, a maximal coverage of 2.6×10^{-11} mol cm^{-2} for a close-packed monolayer of MP-11 adsorbed flat on a perfectly smooth surface,[18] a surface area enhancement of 110 per μm of film thickness can be calculated. This value is noticeably higher than that indirectly determined from the electrode capacitance experiments (66 μm^{-1}), pointing out an excess surface concentration that might be explained by a nonflat adsorption of MP-11 on the metal oxide or by the formation of some MP-11 aggregates within the porous structure of GLAD ITO.

The well-defined linear relationships found between γ_{sat} and film thickness (Figure 3C) and between film capacitance density and film thickness (Figure 2C) strongly support a homogeneous distribution of absorbed molecules throughout the film and, consequently, a homogeneous porosity across the film (within the thickness range explored).

Spectroelectrochemistry. For the spectroelectrochemical studies, the following adsorption conditions were selected: 1 h MP-11 adsorption by immersion of GLAD ITO electrodes in a 50 μM Fe^{III}-MP-11 solution, followed by 15 min desorption of poorly adsorbed MP-11 in a protein-free buffer solution. To check if the overall adsorbed Fe^{III}-MP-11 can be reversibly and quantitatively reduced into Fe^{II}-MP-11 within the GLAD ITO electrodes, the spectroelectrochemical titration of adsorbed MP-11 was performed in the absence of molecular oxygen (i.e., under argon atmosphere). This was achieved by monitoring the film absorbance change (at λ = 419 nm) during a slow cathodic cyclic potential scan (5 mV s^{-1}) (Figure 4B).

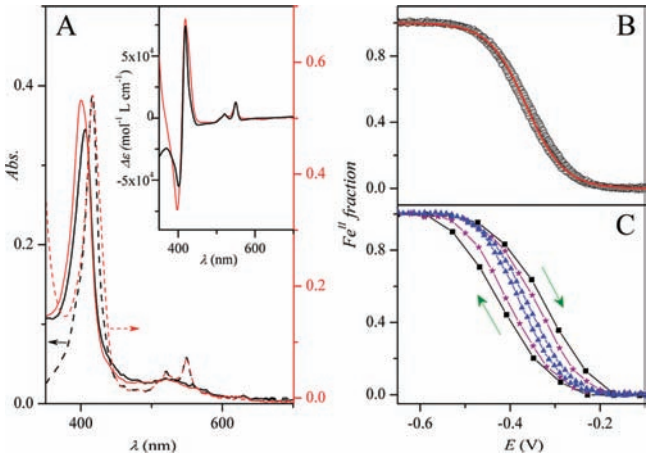

Figure 4. (A) UV−visible blank corrected spectra of (plain lines) oxidized and (dashed lines) reduced MP-11 in (red) homogeneous solution (4 μM; quartz cell of 1-cm path length) and (black) absorbed in a GLAD ITO film ($C^0_{f,MP\text{-}11}$ = 55 mM, l = 1 μm). Inset: difference spectra (reduced minus oxidized) of (red) MP-11 in solution and (black) adsorbed in the GLAD ITO film. (B) Variation of the fraction of Fe^{II} (calculated from the absorbance change at 419 nm) during a cyclic potential scan applied to the MP-11-loaded GLAD ITO film in A (ν = 0.005 V s^{-1}). The experimental data were fitted to the Nernst equation using the following parameters: $E^{0\prime}$ = −0.364 V and n = 0.57. (C) Same as in panel B but for other scan rates: (blue ▲) 0.1, (purple ★) 0.5 and (■)1 V s^{-1}.

The absorbance change follows a typical reversible sigmoid curve, where the forward and reverse traces as a function of potential are nearly overlaid. This is characteristic of a reversible one-electron transfer process where all species reach thermodynamic equilibrium with the electrode within the time scale of the experiment. It is interesting to note that the thermodynamic equilibrium is also reached at shorter time scale since upon raising the scan rate to 0.1 V s^{-1}, the forward and reverse S-shaped absorbance change remains nearly overlaid (Figure 4C). At higher scan rates, however, an increasing potential separation between the S-shaped curve of the forward and reverse scans was observed, reflecting a progressive kinetic control by the heterogeneous electron transfer process from the immobilized MP-11. At slow scan rates, the S-shaped titration curves can thus be fitted to a Nernst equation, yielding from the best fit (Figure 4B) to a formal potential of $E^{0\prime}$ = −0.364 V versus Ag/AgCl and an apparent value of n_{app} = 0.6 electron. The $E^{0\prime}$ is in good agreement with that of −0.38 V determined for the reversible one-electron Fe^{III}/Fe^{II} couple of MP-11 in

dx.doi.org/10.1021/ja301193s | J. Am. Chem. Soc. 2012, 134, 6834−6845

homogeneous solution at pH 7,[23] and similar to the one previously determined by us for MP-11 adsorbed in 250 nm thick GLAD ITO film.[18,26] Also, as previously shown, the value of n_{app} is significantly lower than the ideal value of one. This can be attributed to a nonideal electrochemical behavior resulting from MP-11 distribution in various microenvironments and/or orientations in the ITO film.[26,27] During the starting (−0.05 V) and reverse (−0.65 V) cyclic scans of potentials, the UV−visible absorption spectra of the entirely oxidized (Fe^{III}-heme) and completely reduced (Fe^{II}-heme) MP-11 in the ITO film were recorded and then compared with those obtained in homogeneous solution (Figure 4A).

The good agreement between the spectra of adsorbed MP-11 and those of MP-11 in homogeneous solution, as well as the close similarity in their difference spectra (inset of Figure 4A), clearly shows that the optical properties of adsorbed MP-11 remain the same as that in homogeneous solution, whatever the oxidation state. This result suggests that the physical adsorption of MP-11 within the nanoporous structure of ITO does not significantly affect the coordination sphere and/or geometry of MP-11, and thus, probably its native 3D-structure (i.e., no significant protein denaturation, heme dissociation and/or ligand exchange). It also indicates that all of the MP-11 molecules adsorbed in the ITO film can reversibly exchange their electron through direct electron transfer with the conductive matrix (no need of a redox mediator). Finally, the above experiments demonstrate that, from the variation of absorbance, the amount (or fraction) of oxidized and/or reduced MP-11 can be accurately known and quantitatively determined at each potential (or time) throughout a cyclic scan.

Cyclic Voltammetry and Voltabsorptometry. The dynamics of redox function of MP-11/GLAD ITO films (film thickness of l = 1 μm) were concurrently monitored by cyclic voltammetry and UV−visible spectroscopy. For such purpose, experiments were carried out at various cyclic scan rates during which the absorbance change was simultaneously recorded at 400, 419, and 550 nm (these wavelengths corresponds to the maximum extinction coefficient variations in the Fe^{II} minus Fe^{III} spectrum shown in the inset of Figure 4A, that is, $\Delta\varepsilon_{400}$ = −55 000 M^{-1} cm^{-1}, $\Delta\varepsilon_{419}$ = 80 000 M^{-1} cm^{-1}, and $\Delta\varepsilon_{550}$ = 13 000 M^{-1} cm^{-1}). The resulting variations of absorbance as a function of time, and therefore potential, were used to plot cyclic voltabsorptograms (CVAs) and their respective derivatives (DCVAs).[28,29] The latter are more convenient for direct comparison with cyclic voltammograms (CVs) since they reflect the change in population of redox species with time (and potential) and thus the magnitude of faradaic current in cyclic voltammetry according to the following flux density ϕ (mol cm^{-2} s^{-1}):

$$\phi = \frac{dA_\lambda}{\Delta\varepsilon_\lambda\, dt} = \frac{v\, dA_\lambda}{\Delta\varepsilon_\lambda\, dE} = \frac{i}{nFS} \quad (1)$$

where A_λ is the absorbance change at λ (nm), $\Delta\varepsilon_\lambda$ is the extinction coefficient difference between the reduced and oxidized states, v is the scan rate, n is the number of electrons involved in the redox reaction (here n = 1), S is the projected electrode area, and F is the Faraday constant. A typical set of data recorded at 50 mV s^{-1} are shown in Figure 5, first in the absence of oxygen (left graphs), and subsequently after bubbling pure molecular oxygen up to saturation (right graphs). Under absence of oxygen, the CVA shows a pair of superimposed sigmoid curves which after derivation leads to a well-defined pair of symmetrical peaks (with a peak-to-peak separation close to 0 mV, as expected for an ideal surface-controlled reversible electrochemical process) centered on a formal potential of −0.36 V (Figure 5C), characteristic of the Fe^{III}/Fe^{II} couple of MP-11. The DCVA trace is analogous to the one concomitantly recorded in CV (Figure 5D), except that it is free from the high capacitive background current observed in CV. After subtraction of the capacitive background current (i.e., by subtraction of a blank CV recorded before MP-11 adsorption), the resulting faradaic flux density ϕ on the CV (Figure 5D) was finally comparable to the one obtained in DCVA (showing same peak shapes and also same reduction and oxidation peak potentials). The less ideal response in CV than in DCVA well illustrates the difficulty to precisely deconvolute the faradaic response of a protein film from the high background capacitive current. Nevertheless, the quantitative agreement between the CV and DCVA curves confirms the ability to efficiently cross-correlate the electrochemical and spectroscopic data.

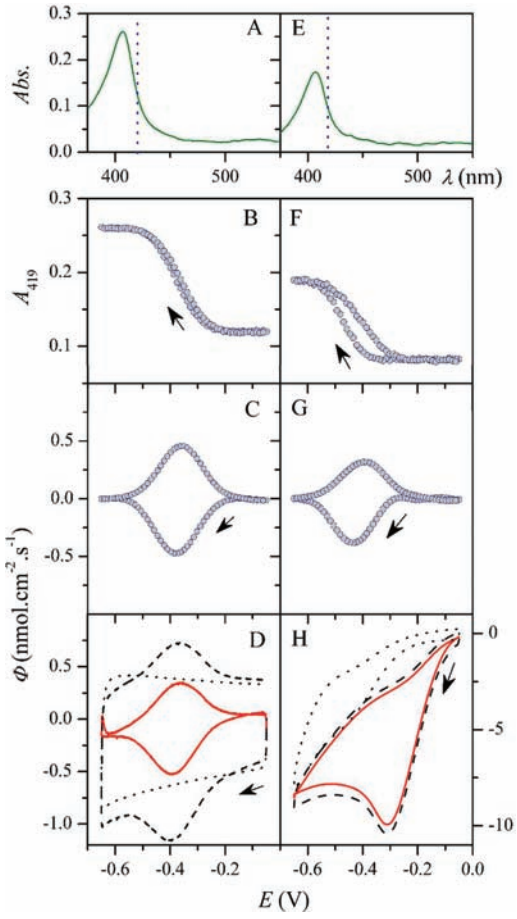

Figure 5. Series of voltammetric and voltabsorptometric experiments (v = 0.05 V s^{-1}) simultaneously recorded at a MP-11-loaded GLAD ITO electrode (l = 1 μm). Left: under argon bubbling and $C^0_{f,MP\text{-}11}$ = 36 mM. Right: under O_2 bubbling (theoretically 1.4 mM of O_2 at saturation under 1 atm) and $C^0_{f,MP\text{-}11}$ = 27 mM (Hepes buffer, pH 7, T = 25 °C). (A and E) UV−visible absorbance spectra recorded just before the cyclic potential scans. (B and F) CVAs monitored at 419 nm ($\Delta\varepsilon_{419}$ = 80 000 M^{-1} cm^{-1}) and their corresponding (C and G) DCVAs and (D H) CVs recorded (dotted line) before and (dashed line) after absorption of MP-11 in the GLAD ITO electrode. CV (red solid line) corrected from the blank CV (i.e., corrected from the dotted line in panel D).

dx.doi.org/10.1021/ja301193s | J. Am. Chem. Soc. 2012, 134, 6834−6845

The analysis of the cathodic and anodic peak intensities in both DCVA and CV as a function of v shows a linear dependence up to a scan rate of 1 V s^{-1} (see Figure S1), whereas the peak areas remain constant and independent of v up to a few volts per second. All of these observations are characteristic of a thin-layer redox process during which all MP-11 molecules in the ITO film are rapidly switched into their reduced or oxidized state within the time scale of the experiment. Concomitantly to the linear increase of peak intensities as a function of v, an exponential increase of the peak-to-peak potential separation was observed. This behavior points out to an increasing kinetic control by the interfacial electron transfer occurring between MP-11 and ITO. It also provides the opportunity to determine the standard heterogeneous electron transfer rate constant, k^0, as well as the charge transfer coefficient α. This was achieved from the plot of the peak-to-peak potential separation in DCVAs as a function of v (Figure S1) and its fit to the theoretical curves calculated from the classical Butler−Volmer equations under thin-layer conditions. From the best fit, values of k^0 = 10 s^{-1} and α = 0.4 were obtained. These values are identical to the ones previously determined for a thinner film of 250 nm GLAD ITO,[18] demonstrating the independence of k^0 with film thickness. This independence also indicates that the electron transport through the nanoporous metal oxide film is not rate limiting (at least up to a few V s^{-1}).

In presence of O_2, the cathodic reversible wave of MP-11 in cyclic voltammetry is converted into a strongly enhanced (by a factor ∼20) irreversible reduction peak, positively shifted by more than 300 mV compared with the irreversible reduction wave of O_2 recorded at a free-MP-11 GLAD ITO electrode (Figure 5H). Such a behavior is characteristic of an efficient interfacial catalytic reduction of O_2 by MP-11 in which the diffusion rate of O_2 is to some degree rate-limiting.[30] The DCVA, simultaneously recorded at 419 nm (Figure 5G), is in marked contrast to the catalytic CV response. In the presence of O_2, a reversible wave remains observable but with a noticeable shift (∼60 mV) of the cathodic peak potential to more negative values. Such a result is a good illustration that in CV the monitored species is not the same as in DCVA. For the former, this is the flux of electrons flowing through the electrode that is measured (here amplified by the catalysis), whereas for the latter, this is the change in proportion of Fe^{II}-MP-11 into the film that is recorded. The DCVA reduction peak observed under catalytic conditions thus corresponds to the flux of Fe^{II}-MP-11 that grows up and accumulates into the ITO film once the concentration of oxygen at the electrode interface is strongly depleted by catalysis (Figure 5). The potential delay at which Fe^{II}-MP-11 starts to accumulate into the film is thus directly related to the rate of oxygen consumption and therefore to the combined rates of the catalytic reaction with O_2 and the O_2 mass transport. The potential delay is thus expected to be modulated through a change of v. Therefore, a series of CVs and CVAs were recorded under the same catalytic conditions but for various scan rates (Figure 6). As expected, the normalized CVA curves (Figure 6A) demonstrate that as v is raised, the forward S-shaped reduction curve is increasingly shifted to negative potential values, and even completely disappears at sufficiently high scan rates, whereas for the reverse scan, the S-shaped curve is progressively converted into a peak-shaped one, leading thus to an odd hysteresis effect.

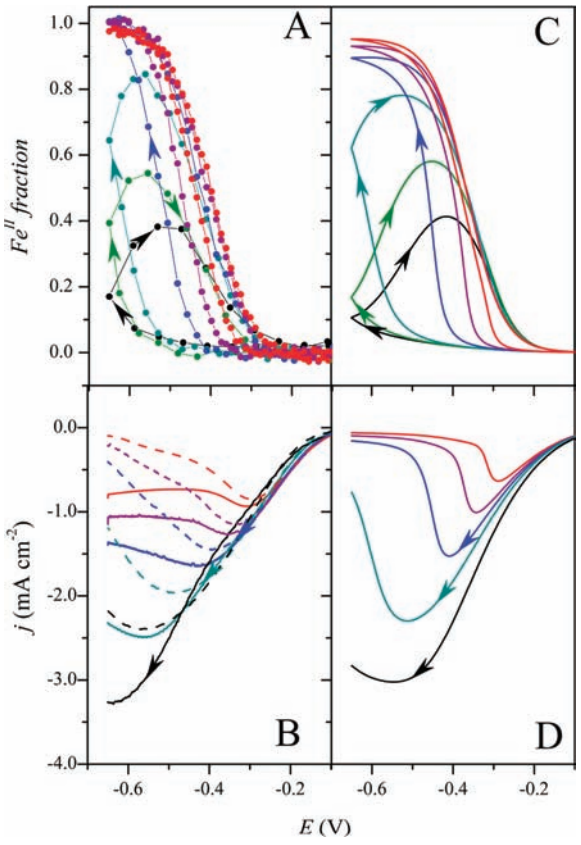

Figure 6. (Left) Experimental (A) CVAs and (B) CVs (for clarity, only the forward sweep is shown) recorded at a MP-11/GLAD ITO electrode (l = 1 μm) in a saturated O_2 solution. Scan rate (V s^{-1}) and MP-11 film concentration (mM) were: (black circles) 1 and 32.5, (green circles) 0.8 and 31, (teal circles) 0.5 and 29, (blue circles) 0.2 and 28, (purple circles) 0.1 and 27, and (red circles) 0.05 and 26. In panel B, the CVs were corrected by subtracting blanks recorded (plain lines) in the absence of MP-11 and O_2 and (dashed lines) in the absence of MP-11 but presence of saturated O_2. (Right) Numerical simulations of (C) CVAs and (D) CVs using the following parameters: $E^{0\prime}$ = −0.36 V, k^0 = 10 s^{-1}, α = 0.4, n_{app} = 0.6, n = 2, D_{O_2} = 2 × 10^{-5} cm^2 s^{-1}, C_{O_2} = 1.4 mM, K_{O_2} = 70, k_1 = 5 × 10^3 M^{-1} s^{-1}, k_2 = 11 s^{-1}, l = 1 μm. Values of D_{O_2} and C_{O_2} were from ref 31 and $C^0_{f,MP\text{-}11}$ were those determined experimentally.

It is worth noting that, before the addition of oxygen, only a small fraction of MP-11 was observed to be continuously released into the electrochemical cell by slow desorption from the ITO film. This was evidenced by a slight decrease of the Fe^{III} Soret band intensity recorded after each cyclic scan. It was estimated that a fraction of ∼1−2% of MP-11 is desorbed after each scan (Figure S2), which is negligible as long as the number of repetitive potential scans or immersion time of MP-11-loaded GLAD ITO electrode in the electrochemical cell is limited. However, in the presence of oxygen, the percentage loss of MP-11 per cyclic scan was observed to be significantly higher, indicating a Soret-band absorbance decrease of 3−6% per scan (Figure S2). This observation indicates that, under catalytic turnover conditions, an additional fraction of MP-11 is irreversibly lost. This was attributed to the reactive oxygenated byproducts (H_2O_2, $HO_2^{\bullet-}$, $OH^{\bullet}$) generated during the catalytic reduction of O_2, which could irreversibly damage the MP-11 (e.g., by reaction with the unsaturated sites of the porphyrin ring). For precise analysis of the experimental data, the MP-11

dx.doi.org/10.1021/ja301193s | J. Am. Chem. Soc. 2012, 134, 6834−6845

film concentration was therefore systematically recalculated from the Soret band absorbance determined after each CV/CVA scan.

The background subtracted catalytic reduction waves (plain lines) reported in Figure 6B (for clarity, only the forward CV scan is shown) are far from ideal electrocatalytic CV responses. The waves are indeed relatively large and ill-defined with a tendency to hang out, rendering their precise interpretation and analysis difficult. Such a behavior is not really surprising because the direct reduction of O_2 may interfere in the end range of the cathodic potential sweep, and also the catalytically generated reactive oxygenated species (ROS), such as H_2O_2, may be further reduced within the potential window where the catalytic reduction of O_2 by MP-11 occurs. These additional reactions should thus significantly contribute and interfere to the overall faradaic current response. To roughly evaluate the contribution of direct O_2 reduction in the overall catalytic responses, the catalytic waves in Figure 6B were also reported (dashed lines) after subtraction of the blank CV responses recorded beforehand in the presence of O_2 but absence of MP-11 (Figure 6B). The corrected curves show significant difference between the different type of blank subtracted responses and this once more again illustrates the difficulty to deconvolute the catalytic response of interest from the nonrelated capacitive and faradaic background responses. The true catalytic response is certainly somewhere between these two background subtracted waves. This problem does not exist in DCVA since only the MP-11 absorbance change is monitored.

Theoretical Analysis and Simulation. The question we would like now to address is what type of catalytic mechanism can we propose to rationalize and predict the overall voltammetric and voltabsorptometric experimental curves reported in Figure 6, and also what mechanistic and kinetic information can we extract from such experimental data? To try to answer this question, we have investigated the possibility to predict the CV and CVA curves through the numerical resolution of the differential equation rates of diffusion-reaction that prevail at the GLAD ITO interface within the framework of a plausible mechanism of catalytic reduction of O_2 by MP-11.

An overview of the different possible catalytic reaction pathways is gathered in Scheme 1. Starting from the native Fe^{III}-MP-11, the first step consists to electrochemically reduce the Fe^{III}-heme into a Fe^{II}-heme. The rate of this heterogeneous one-electron transfer can be described by the Butler−Volmer formalism and its associated electrochemical parameters (i.e., $E^{0\prime}$, α, and k^0). Following this reduction step and in accordance with the usually proposed catalytic reduction of oxygen by iron porphyrins,[32] the electrochemically generated Fe^{II} is expected to bind O_2 reversibly via an inner-sphere mechanism, leading thus to the formation of a $Fe^{II}-O_2$ (or $Fe^{III}-O_2^{\bullet-}$). The kinetics of this binding reaction can be defined by a forward bimolecular binding rate constant, k_1, and a backward first-order rate dissociation constant, k_{-1}. According to its high degree of oxidation state, the $Fe^{II}-O_2$ intermediate is expected to be rapidly electrochemically reduced at the potential where MP-11 is reduced, to lead after protonation to the hydroperoxo species $Fe^{III}-OOH$ (compound 0). After that, the hydroperoxo intermediate may undergo either: (i) heterolytic cleavage of the O−O bond to produce an oxyferryl radical cation (i.e., $[Fe^{IV}{=}O]^{\bullet+}$ or compound I) and H_2O, (ii) homolytic cleavage of the O−O bond to generate an oxyferryl compound (i.e., $Fe^{IV}{=}O$ or compound II) and highly reactive $OH^{\bullet}$ radicals, and (iii) release of the hydroperoxo ligand to regenerate the resting Fe^{III} species and hydrogen peroxide.[33] The three possible pathways ensuing from the intermediate $Fe^{III}-OOH$ finally allow definition of 3 different catalytic loops, each having its own electron stoichiometry of 2, 3, and 4.

In addition to these catalytic reactions, a Fenton-like reaction between H_2O_2 and Fe^{II}-MP-11 can be envisioned and the ROS species (H_2O_2, $HO_2^{\bullet-}$, $OH^{\bullet}$, ...) generated from this reaction or from catalysis may further react with the electrode or MP-11, the latter leading to an irreversible damage of the catalyst, as previously noticed. The formation of ROS is however a minor oxygen reduction pathway. This assertion is based on the observation that, even for the lower scan rates of 0.05 V s^{-1}, less than 5% of the catalyst is lost during each cyclic voltammetric experiments (Figure S2). According to this argument, we have found it to be reasonable to exclude the 3-e^--based catalytic loop from the main catalytic reaction pathways to finally restrict the possibilities to 2- or 4-e^--based catalytic processes, the first one leading the production of hydrogen peroxide and the second one to water. Moreover, whatever the 2- or 4-e^--reaction scheme, we have considered the last step (i.e., regeneration of the resting Fe^{III} state) as the rate-determining reaction of catalysis and thus the overall preceding chemical or electrochemical reactions are much faster. Under these conditions, the two catalytic loops based on 2- or 4-electron transfers can be appropriately described by the simplified and unified catalytic reaction scheme shown in Scheme 2. Notice that in this reaction scheme, the back dissociation of O_2 (k_{-1}) is neglected according to the hypothesis that the heterogeneous electron transfer reaction that follows the formation of $Fe^{II}-O_2$ is fast. An important advantage of this simplified reaction scheme is that it can be described with a reduced number of tractable parameters, that is, the rate constants k_1 and k_2; the electrochemical parameters $E^{0\prime}$, α, and k^0; and the mass transport parameters of O_2, therefore, considerably simplifying simulations and kinetics analysis.

Simulations of CVs and CVAs were thus done on the basis of the catalytic reaction mechanism in Scheme 2 (schematically represented as occurring homogeneously inside the porous conductive film, and across which the gradients of O_2 concentration take place perpendicularly to the electrode) and on the numerical resolutions of the set of partial derivative equations and boundary conditions given below. For

Scheme 1. Overview of Plausible Catalytic Reaction Pathways for the Reduction of O_2 by MP-11[a]

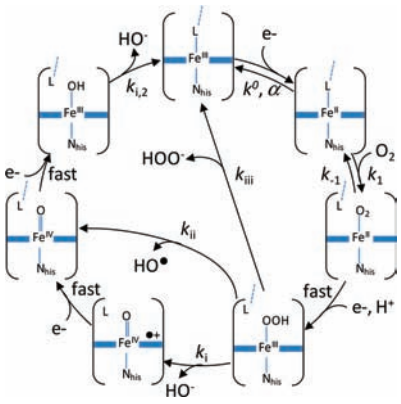

[a]The ligand L is assumed to be the amino residue of either the terminal lysine or of Val_{10} of a neighbouring MP-11.

dx.doi.org/10.1021/ja301193s | J. Am. Chem. Soc. 2012, 134, 6834−6845

Scheme 2. Schematic Overview of the General Catalytic Reaction Scheme of Reduction of O_2 by MP-11 and Gradients of O_2 Concentration Occurring within the Nanoporous GLAD ITO Film[a]

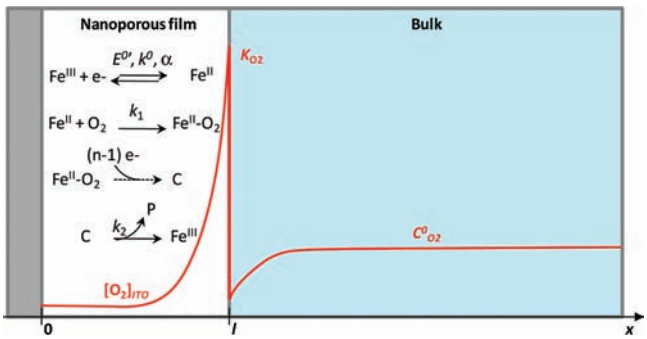

[a]C corresponds either to the Fe^{III}−OOH or the Fe^{III}−OH intermediate according to the 2-e^- or 4-e^- pathway, respectively. P corresponds either to H_2O_2 or HO^-/H_2O.

simplification, we have treated the nanoporous film of ITO as a continuum within which the concentration of MP-11 ($C^0_{f,MP\text{-}11}$) is homogenously distributed, the molecule of oxygen is free to diffuse (i.e., same diffusion coefficient in the film than in the bulk of solution), and the Fick's second law modified by appropriate kinetic terms applies. With the aim to take into account the fact that the electrons are rapidly transported across the conductive GLAD ITO film, and so that such electron transport is not rate-limiting, we have considered that it could be analogous to that obtained with a MP-11 able to diffuse rapidly across the film (i.e., by introducing into the numerical simulation a sufficiently high film-diffusion coefficient of MP-11, e.g., $\geq 10^{-4}$ cm^2 s^{-1}, in such a way that the mass transport of this process, equivalent to an electron transport trough the film, is not rate-determining).

At the electrode surface, $x = 0$, the flux of electrons that flow through the interface is given by the addition of the two currents i_1 and i_2, the first one being related to the relatively slow initial one-electron transfer centered on the Fe^{III}/Fe^{II} couple and the second one to the fast multiple-heterogeneous electron transfers that follow the formation of Fe^{II}−O_2.

$$\frac{i}{FS} = \frac{i_1}{FS} + \frac{i_2}{FS} = -D_{MP}\left(\frac{\partial[Fe^{II}]}{\partial x}\right)_{x=0} - (n-1)D_{MP}\left(\frac{\partial[C]}{\partial x}\right)_{x=0} = D_{MP}\left(\frac{\partial[Fe^{III}]}{\partial x}\right)_{x=0} + (n-1)D_{MP}\left(\frac{\partial[Fe^{II}-O_2]}{\partial x}\right)_{x=0} \quad (2)$$

Here, $[Fe^{III}]$, $[Fe^{II}]$, $[Fe^{II}$−$O_2]$, and [C] are the volumic film concentrations of the different oxidation states of MP-11, n is the stoichiometric number of electrons involved in the catalytic cycle (i.e., 2 or 4 as discussed above), and D_{MP} is the artificially high film diffusion coefficient of MP-11 that allows mimicking fast electron transport across the conductive film. If we assume that the first electron transfer rate centered on the Fe^{III}/Fe^{II} couple obeys the Butler−Volmer law, we can write:

$$\frac{i_1}{FS} = -D_{MP}\left(\frac{\partial[Fe^{II}]}{\partial x}\right)_{x=0} = D_{MP}\left(\frac{\partial[Fe^{III}]}{\partial x}\right)_{x=0} = k^0 \exp\left[-\alpha\frac{n_{app}F}{RT}(E - E^{0'})\right][Fe^{III}]_{x=0} - k^0 \exp\left[(1-\alpha)\frac{n_{app}F}{RT}(E - E^{0'})\right][Fe^{II}]_{x=0} \quad (3)$$

Starting with the reduction, as is the case here, the electrode potential is scanned linearly in the cathodic direction at a scan rate v from an initial potential E_i up to a potential E_f. The latter corresponds to a time t_R where the scan is reversed and goes back to the initial potential at the same scan rate v:

$$0 \leq t \leq t_R: E = E_i - vt$$

$$t_R \leq t \leq 2t_R: E = E_f + v(t - t_R) = 2E_f - E_i + vt$$

For the substrate,

$$\left(\frac{\partial[O_2]}{\partial x}\right)_{x=0} = 0 \quad (4)$$

Inside the film, $0 \leq x \leq l$, concentration changes of the various forms of MP-11 with time are given by the following differential equations:

$$\frac{\partial[Fe^{III}]}{\partial t} = D_{MP}\frac{\partial^2[Fe^{III}]}{\partial x^2} + k_2[C] \quad (5)$$

$$\frac{\partial[Fe^{II}]}{\partial t} = D_{MP}\frac{\partial^2[Fe^{II}]}{\partial x^2} - k_1[Fe^{II}][O_2] \quad (6)$$

$$\frac{\partial[Fe\text{-}O_2]}{\partial t} = D_{MP}\frac{\partial^2[Fe\text{-}O_2]}{\partial x^2} + k_1[Fe^{II}][O_2] \quad (7)$$

$$\frac{\partial[C]}{\partial t} = D_{MP}\frac{\partial^2[C]}{\partial x^2} - k_2[C] \quad (8)$$

$$\frac{\partial[O_2]}{\partial t} = D_{O_2}\frac{\partial^2[O_2]}{\partial x^2} - k_1[Fe^{II}][O_2] \quad (9)$$

where $[O_2]$ and D_{O_2} are, respectively, the concentration and diffusion coefficient of O_2 into the film (as already mentioned, D_{O_2} was considered the same in the film and in the homogeneous solution, that is, $D_{O_2} = 2 \times 10^{-5}$ cm^2 s^{-1}).[31]

The mass balance equation of the different forms of MP-11 into the film is given by:

$$C^0_{f,MP\text{-}11} = [Fe^{III}] + [Fe^{II}] + [Fe^{II}\text{-}O_2] + [C]$$

As it will be discussed later, at the film/solution boundary, $x = l$, partitioning of O_2 at the solution/film interface has to be taken into account:

$$[O_2]_{x=l^-} = K_{O_2}[O_2]_{x=l^+} \quad (10)$$

where $[O_2]_{x=l^-}$ corresponds to the concentration of O_2 in the void fraction of the porous ITO film and K_{O_2} represents the O_2 solution/film partition coefficient.

At the film/solution boundary, we have also:

dx.doi.org/10.1021/ja301193s | J. Am. Chem. Soc. 2012, 134, 6834−6845

$$D_{O_2}\left(\frac{\partial[O_2]}{\partial x}\right)_{x=l^-} = D_{O_2}\left(\frac{\partial[O_2]}{\partial x}\right)_{x=l^+} \quad (11)$$

In solution, the diffusion of O_2 is given by:

$$\frac{\partial[O_2]}{\partial t} = D_{O_2}\frac{\partial^2[O_2]}{\partial x^2} \quad (12)$$

Far from the electrode, the concentration of O_2 is constant and represented by $C^0_{O_2}$, and for the initial conditions at $t = 0$ we have in the film:

$$[O_2]_{t=0} = K_{O_2}C^0_{O_2} \quad (13)$$

$$[Fe^{III}]_{t=0} = C^0_{f,MP\text{-}11} \quad (14)$$

$$[Fe^{II}]_{t=0} = 0 \quad (15)$$

$$[C]_{t=0} = 0 \quad (16)$$

According to the fast electron transport throughout the film (represented here by the high diffusion rate of the overall MP-11 species into the film) and the fast multistep electron transfers/chemical reactions that lead to the conversion of Fe^{II}–O_2 into C, the concentration profiles of the different forms of MP-11 are expected to be flat and the film concentration of Fe^{II}–O_2 close to zero. It is worth noting that the flat profile concentrations of MP-11 do not mean that the O_2 gradient in the film is flat. Therefore, we have the following approximations:

$$[Fe^{II}\text{-}O_2] = 0$$

$$C^0_{f,MP\text{-}11} \approx [Fe^{III}] + [Fe^{II}] + [C] \quad (17)$$

as well as a simplification of set of differential eqs 5–9:

$$\frac{\partial[Fe^{III}]}{\partial t} = D_{MP}\frac{\partial^2[Fe^{III}]}{\partial x^2} + k_2[C] \quad (18)$$

$$\frac{\partial[Fe^{II}]}{\partial t} = D_{MP}\frac{\partial^2[Fe^{II}]}{\partial x^2} - k_1[Fe^{II}][O_2] \quad (19)$$

$$\frac{\partial[C]}{\partial t} = D_{MP}\frac{\partial^2[C]}{\partial x^2} - k_2[C] + k_1[Fe^{II}][O_2] \quad (20)$$

$$\frac{\partial[O_2]}{\partial t} = D_{O_2}\frac{\partial^2[O_2]}{\partial x^2} - k_1[Fe^{II}][O_2] \quad (21)$$

Since we have assumed a flat concentration profile for the MP-11 species into the film, we can thus write for the flux of currents:

$$\frac{i_1}{FS} \approx -l\frac{d[Fe^{III}]}{dt} \quad (22)$$

$$\frac{i_2}{FS} \approx (n-1)l\frac{d[C]}{dt} \quad (23)$$

Derivation of eq 17 leads:

$$-\frac{d[Fe^{III}]}{dt} = \frac{d([Fe^{II}] + [C])}{dt} \quad (24)$$

From combination of eqs 22–24:

$$\frac{i_2}{i_1} = -(n-1)\frac{\frac{d[C]}{dt}}{\frac{d[Fe^{III}]}{dt}} = -(n-1)\frac{\frac{d[C]}{dt}}{\frac{d([Fe^{II}]+[C])}{dt}}$$

and thus

$$\frac{i_2}{i_1} = -(n-1)\frac{[C]}{[Fe^{II}] + [C]}$$

We have finally for the total current the following expression:

$$i = i_1\left\{1 - (n-1)\frac{[C]}{[Fe^{II}] + [C]}\right\} \quad (25)$$

Numerical resolution of the differential eqs 18–21, and 12, using the boundary and initial conditions, allows calculation of the current–potential curves using eqs 3 and 25, as well as the concentration profiles of each species in the ITO film and solution. The simulated CVAs were simply acquired from integration of $[Fe^{II}]$ concentration profile calculated at each potential. From knowledge of $C^0_{O_2}$, $C^0_{f,MP\text{-}11}$ and the independent estimation of D_{O_2}, $E^{0\prime}$, k^0, α, and n_{app}, the four unknown parameters n, k_1, k_2 and K_{O_2} can finally be estimated from an iterative adjustment of their values and fits of the simulated curves to the experimental CVs and CVAs shown in Figure 6. However, since there is a large range of possible values for k_1, k_2 and K_{O_2}, it was necessary to start the iterative process from the finding of a specific limiting case from which a single parameter could be extracted. An interesting limiting case is the steady-state catalytic current response observed during the forward scan of the highest CV scan rate (1 V s^{-1}) in Figure 6B. The plateau-shaped catalytic wave is indeed characteristic of steady-state catalysis where the magnitude of the plateau current is kinetically controlled by the rate-determining step of the catalytic cycle. This steady-state situation is confirmed by the corresponding CVA curve at 1 V/s which shows that the Fe^{II} fraction during the forward scan remains close to nil (the Fe^{II} concentration within the film starts to increase only at the end of the forward scan). Under these conditions, the O_2 concentration at the electrode interface is assumed to be high (saturating concentration) and not too drastically depleted (i.e., the scan rate is fast enough that the oxygen consumption is not too strong), leading to a catalytic plateau current controlled by the regeneration rate of Fe^{III}-MP-11, independent of the O_2 concentration (i.e., k_2 is the rate-determining step). Such limiting conditions finally suggest that the analytical expression of the catalytic plateau current, i_{pl}, is given by:

$$\frac{i_{pl}}{nFS} = k_2 l C^0_{f,MP\text{-}11}$$

This expression is equivalent to the equation of steady-state catalytic plateau current that can be established at a redox monolayer-coated electrode engaged in a catalytic reaction rate-limited by the formation of a precursor complex with a soluble substrate.[7,9,34] From the catalytic plateau current of $i_{pl} \sim 3$ mA/cm^2 in Figure 6B and the spectroscopically determined MP-11 film concentration of 32.5 mM, we calculated, using $l = 1$ μm, a k_2 value of 11 s^{-1} for $n = 2$ and 5.5 s^{-1} for $n = 4$.

After having fixed the value of k_2, a series of CV and CVA curves were then simulated for $n = 2$ and 4 and for different values of k_1 and K_{O_2}. A typical set of simulations carried out at a fixed scan rate of 1.0 and 0.5 V s^{-1} are reported in Figures S3

dx.doi.org/10.1021/ja301193s | J. Am. Chem. Soc. 2012, 134, 6834–6845

and S4 (the simulated parameters $E^{0\prime}$, k^0, α, n_{app} were the same as those experimentally determined under argon and the selected values of k_1, k_2 and K_{O_2} are reported on the graphs). From the simulated curves in Figures S3 and S4, a favorable O_2 partitioning ($K_{O_2} \geq 50$) was required for having catalytic current responses of similar magnitudes than the experimental ones. The favorable O_2 partitioning was also evidenced with the noncatalytic CV response recorded at a free-MP-11 GLAD ITO electrode, and for which the magnitude of the irreversible reduction wave of O_2 was observed to be much higher than at a plain ITO electrode. It is worth noting that the shape of the simulated CVAs was independent of n, whereas the magnitudes of the CV catalytic waves were proportional to n. The influence of k_1 on the magnitudes and shapes of the simulated curves was better discerned on the CVAs (Figures S3 and S4), where both an increasing delays in the Fe^{II} apparition and a boost of Fe^{II} accumulation rate are observed as the value of k_1 is raised. At intermediate scan rates (e.g., 0.5 V s^{-1}) where the most striking hysteresis effect is observed, it is even possible to extract from the shape of a single voltabsorptogram the two kinetic rate constants k_1 and k_2. This can be qualitatively explained as follows: at the beginning of the scan the catalysis is kinetically controlled by k_2 due to the high concentration of O_2 initially present in the film (saturating concentration), but as the O_2 is increasingly depleted to nil by catalysis (Figure 7), the catalysis

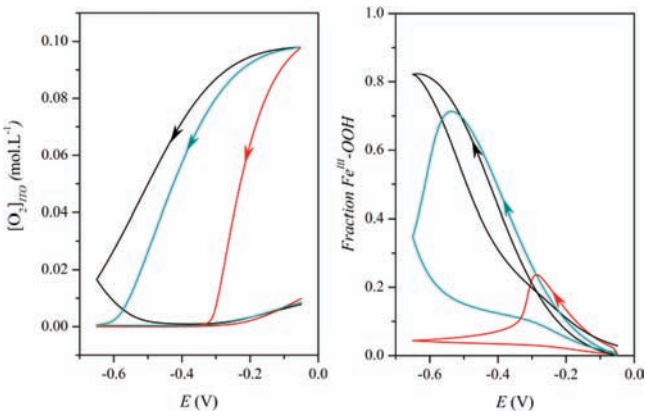

Figure 7. Simulated (left) oxygen film concentration and (right) Fe^{III}–OOH fraction in the GLAD ITO film during the time course of a cyclic potential scan of (red line) 0.05, (teal line) 0.5 and (black line) 1 V.s^{-1}. The simulated parameters are the same as in Figure 6 and the Fe^{III}–OOH fraction and average film concentration of O_2 were obtained from the integration of the film concentration profiles of O_2 and Fe^{III}–OOH.

passes progressively from a kinetic control by k_2 to a kinetic control by $k_1[O_2]_{ITO}$. It should be noted that this analysis was also attempted with k_1 as the rate-determining step (i.e., k_2 is sufficiently high that it cannot be rate-limiting even at high O_2 concentration); however, it was not possible to correctly simulate the experimental CVs and CVAs, regardless of rate constants and other parameters.

Finally, from comparison of the overall experimental CV and CVA curves in Figure 6 to the simulated ones, the most satisfactory results were obtained for the 2-electron mechanism and the following values of parameters: $K_{O_2} = 70$, $k_1 = 5 \times 10^3$ M^{-1} s^{-1} and $k_2 = 11$ s^{-1}.

According to the catalytic loop based on the 2-e- reduction of O_2 by MP-11 (Scheme 1), the intermediate species C which is expected to be accumulated within the ITO network is the Fe^{III}–OOH species (i.e., compound 0). A question one would like to address is whether the transient Fe^{III}–OOH intermediate could be spectroscopically identified and distinctly monitored during a CVA. The CVA curves were obtained from the monitoring of Fe^{II} at 419 and 550 nm and Fe^{III} at 400 nm. When one looks at the experimental CVA plots in Figure S5, the rate of Fe^{II} accumulation correlates very well to the rate of Fe^{III} decrease, suggesting no accumulation of Fe^{III}–OOH. This is in contrast to that predicted from the CVA simulations (Figure 7) which show preponderant accumulation of C (i.e., Fe^{III}–OOH), especially at high scan rates where the O_2 concentration into the film remains relatively high, notably during the forward scan where k_2 rate control the regeneration of Fe^{III} from Fe^{III}–OOH. This outcome can be explained by a high similitude between the UV–visible absorption spectra of Fe^{III}–OOH and the resting Fe^{III} state, preventing thus any spectroscopic differentiation of the two compounds. This is a reasonable hypothesis since both are a hexacoordinated low-spin Fe^{III} heme.[35,36]

■ CONCLUSION

In the present work, we have demonstrated the potential offered by the coupling of cyclic voltammetry with UV–visible absorption spectroscopy for investigating the reactivity of a small redox protein adsorbed in a transparent 3D-nanoporous GLAD ITO electrode. This has been illustrated here with the mechanistic and kinetics analysis of the catalytic reduction of O_2 by microperoxidase-11, but it could be also easily extended to the study of many other redox proteins, enzymes or biomimetic catalysts able to directly exchange an electron with a conductive surface. It could be also applied to systems involving redox-mediated electron transfer. Moreover, according to their excellent conductivity and transparency in the visible, the present spectroelectrochemical methodology is amenable to a coupling with other time-resolved spectroscopic techniques such as resonance Raman, infrared or fluorescence spectroscopy, providing thus the opportunity to develop unique approaches for better understanding complex redox-coupled electron transfer mechanisms involved in redox (bio)molecules. It might also be of great interest for the development and optimization of new spectroelectrochemical sensors and biosensors, or eventually new photoelectrocatalytic systems or biofuel cells.

■ EXPERIMENTAL SECTION

All chemicals were purchased from Sigma Aldrich. For ITO films, an ITO-coated glass substrate was used as the deposition substrate (8–12 Ω/square, Delta Technologies Ltd.). Experimental details concerning the nanoporous film deposition are given elsewhere.[21]

Prior to adsorption, the ITO electrodes were carefully rinsed with ethanol and Milli-Q. water. The geometric electrode surface was delimited to 0.4 ± 0.1 cm^2 by using nail varnish. Adsorption procedures were conducted in a 50 μM MP-11 solution, 10 mM Hepes, pH 7.0, T = 20 °C.

The MP-11 concentration in the void fraction of the porous film is calculated from the following equation (assuming a porosity p of 0.48 and a film thickness l expressed in cm):

$$C^0_{f,\text{MP-11}} = \frac{A_\lambda}{\varepsilon_\lambda p l}$$

Spectroelectrochemical measurements were performed using a thermostatted homemade three-electrode spectroelectrochemical cell.[37] The reference electrode is an Ag/AgCl, 3 M KCl electrode

dx.doi.org/10.1021/ja301193s | J. Am. Chem. Soc. 2012, 134, 6834–6845

(WPI) and the counter electrode is a platinum wire. UV−visible absorption spectroscopic measurements were performed on a HR2000+ diode array spectrometer (Ocean Optics) synchronized with a potentiostat (Autolab). Cyclic voltammetric experiments were systematically performed under ohmic drop compensation in 1.1 mL electrolyte solution (Hepes 90 mM, NaCl 10 mM, pH 7.0) at 20 °C. The spectroelectrochemical cell was carefully degassed for 1 h by argon bubbling prior to measurements. For measurements under saturated oxygen atmosphere, the electrochemical cell was flushed with pure oxygen gas for 30 min prior to measurements, and for a further 2 min between each measurement. The integration time for spectrometric measurements was fixed to 30 ms. Depending on the time resolution required, each data point on a CVA or DCVA can result from the averaging of 2, 4, or 8 spectra. All potentials in the text are referred to the Ag/AgCl, 3 M KCl reference (i.e., +0.2 V vs NHE).

Numerical Computation Procedures. For the numerical resolution of eqs 5−9, an explicit finite difference procedure was used. Space and time were divided into intervals of length Δx and Δt. We designate any of the three concentration variables involved, $[Fe^{III}]$, $[Fe^{II}]$, [C] and $[O_2]$ as [Z]. For time $t = j\Delta t$ $(0 \le j \le n)$ and for $x = i\Delta x$ $(0 \le i \le m)$, the current value of [Z] is noted $[Z]^i_j$. The time and space derivative are replaced by the following finite difference expressions:

$$\frac{\partial[Z]}{\partial t} = \frac{[Z]^i_j - [Z]^i_{j-1}}{\Delta t}$$

$$\frac{\partial^2[Z]}{\partial x^2} = \frac{[Z]^{i+1}_j - 2[Z]^i_j + [Z]^{i-1}_j}{\Delta x^2}$$

allowing the calculation of the actual values (j) from the preceding values $(j-1)$

When nonlinear, the chemical terms are linearized using the preceding values. For example, $[Z] \times [Z']$ is replaced by:

$$0.5([Z]^i_{j-1}[Z']^i_j + [Z]^i_j[Z']^i_{j-1})$$

At each time, the various values of concentration of the 3 forms of MP-11 and $[O_2]$ are related by 4 m equations taking into account boundary equations at the electrode surface and at the film/solution interface.

In the solution, the time and space-dependent concentration of O_2 obeys second Fick's law (eq 12) and it follows that its concentration and gradient at the electrode surface can be calculated from the following integral equation:[38]

$$[O_2]_{x=l^+} = C^0_{O_2} - \frac{\sqrt{D_{O_2}}}{\sqrt{\pi}} \int_0^t \left(\frac{\partial[O_2]}{\partial x}\right)_{x=0} \frac{d\eta}{\sqrt{t-\eta}}$$

where the convolution integral in the latter expression can be approximated by the following expression:

$$\frac{1}{\sqrt{\pi}} \int_0^t \left(\frac{\partial[O_2]}{\partial x}\right)_{x=0} \frac{d\eta}{\sqrt{t-\eta}} \approx \frac{1}{\sqrt{\pi}} \sum_j^{j=n-1} \int_{j\Delta t}^{(j+1)\Delta t} \left(\frac{\partial[O_2]}{\partial x}\right)_{x=0} \frac{d\eta}{\sqrt{n\Delta t - \eta}}$$

A classical matrix inversion procedure is used for the resolution of the 4 m equations, which is repeated for all n.

Typical values of n and m for the simulation of a cyclic voltammetric curve are n = 1000 and m = 20.

■ ASSOCIATED CONTENT

Supporting Information

Complementary data, simulations. This material is available free of charge via the Internet at http://pubs.acs.org.

■ AUTHOR INFORMATION

Corresponding Author

veronique.balland@univ-paris-diderot.fr; limoges@univ-paris-diderot.fr

Notes

The authors declare no competing financial interest.

■ ACKNOWLEDGMENTS

This work was supported by Agence Nationale pour la Recherche (ANR 3D-BIOELEC project). R.T.T. and M.J.B. acknowledge funding from NSERC, Micralyne, and Alberta Innovates: Technology Futures.

■ REFERENCES

(1) Willner, I.; Katz, E. *Angew. Chem., Int. Ed.* **2000**, *39*, 1180−1218.
(2) Armstrong, F. A.; Wilson, G. S. *Electrochim. Acta* **2000**, *45*, 2623−2645.
(3) Newman, J.; Setford, S. *Mol. Biotechnol.* **2006**, *32*, 249−268.
(4) Cracknell, J. A.; Vincent, K. A.; Armstrong, F. A. *Chem. Rev.* **2008**, *108*, 2439−2461.
(5) Ronkainen, N. J.; Halsall, H. B.; Heineman, W. R. *Chem. Soc. Rev.* **2010**, *39*, 1747−1763.
(6) Léger, C.; Elliott, S. J.; Hoke, K. R.; Jeuken, L. J. C.; Jones, A. K.; Armstrong, F. A. *Biochemistry* **2003**, *42*, 8653−8662.
(7) Léger, C.; Bertrand, P. *Chem. Rev.* **2008**, *108*, 2379−2438.
(8) Armstrong, F. A. *J. Chem. Soc., Dalton Trans.* **2002**, 661−671.
(9) Savéant, J.-M. *Elements of Molecular and Biomolecular Electrochemistry*; Wiley-Interscience: New York, 2006.
(10) Kemp, G. L.; Marritt, S. J.; Xiaoe, L.; Durrant, J. R.; Cheesman, M. R.; Butt, J. N. *Biochem. Soc. Trans.* **2009**, *37*, 368−372.
(11) Ash, P. A.; Vincent, K. A. *Chem. Commun.* **2012**, *48*, 1400−1409.
(12) Astuti, Y.; Topoglidis, E.; Briscoe, P. B.; Fantuzzi, A.; Gilardi, G.; Durrant, J. R. *J. Am. Chem. Soc.* **2004**, *126*, 8001−8009.
(13) Marritt, S. J.; Kemp, G. L.; Xiaoe, L.; Durrant, J. R.; Cheesman, M. R.; Butt, J. N. *J. Am. Chem. Soc.* **2008**, *130*, 8588−8589.
(14) Murgida, D. H.; Hildebrandt, P. *Chem. Soc. Rev.* **2008**, *37*, 937−945.
(15) Wisitruangsakul, N.; Zebger, I.; Ly, K. H.; Murgida, D. H.; Ekgasit, S.; Hildebrandt, P. *Phys. Chem. Chem. Phys.* **2008**, *10*, 5276−5286.
(16) Topoglidis, E.; Campbell, C. J.; Cass, A. E. G.; Durrant, J. R. *Langmuir* **2001**, *17*, 7899−7906.
(17) McKenzie, K. J.; Marken, F. *Langmuir* **2003**, *19*, 4327−4331.
(18) Renault, C.; Harris, K. D.; Brett, M. J.; Balland, V.; Limoges, B. *Chem. Commun.* **2011**, *47*, 1863−1865.
(19) Robbie, K.; Friedrich, L. J.; Dew, S. K.; Smy, T.; Brett, M. J. *J. Vac. Sci. Technol., A* **1995**, *13*, 1032−1035.
(20) Robbie, K.; Sit, J. C.; Brett, M. J. *J. Vac. Sci. Technol., B* **1998**, *16*, 1115−1122.
(21) Krause, K. M.; Taschuk, M. T.; Harris, K. D.; Rider, D. A.; Wakefield, N. G.; Sit, J. C.; Buriak, J. M.; Thommes, M.; Brett, M. J. *Langmuir* **2009**, *26*, 4368−4376.
(22) Krause, K. M.; Vick, D. W.; Malac, M.; Brett, M. J. *Langmuir* **2010**, *26*, 17558−17567.
(23) Marques, H. M. *Dalton Trans.* **2007**, 4371−4385.
(24) Harbury, H. A.; Loach, P. A. *Proc. Natl. Acad. Sci. U.S.A.* **1959**, *45*, 1344−1359.
(25) Wilson, M. T.; Ranson, R. J.; Masiakowski, P.; Czarnecka, E.; Brunori, M. *Eur. J. Biochem.* **1977**, *77*, 193−199.
(26) Balland, V.; Lecomte, S.; Limoges, B. *Langmuir* **2009**, *25*, 6532−6542.
(27) Murgida, D. H.; Hildebrandt, P. *J. Mol. Struct.* **2001**, *565*−*566*, 97−100.
(28) Bancroft, E. E.; Sidwell, J. S.; Blount, H. N. *Anal. Chem.* **1981**, *53*, 1390−1394.

(29) Bowden, E. F.; Hawkridge, F. M.; Chlebowski, J. F.; Bancroft, E. E.; Thorpe, C.; Blount, H. N. *J. Am. Chem. Soc.* **1982**, *104*, 7641−7644.
(30) Andrieux, C. P.; Savéant, J.-M. *J. Electroanal. Chem.* **1978**, *93*, 163−168.
(31) CRC. *Handbook of Chemistry and Physics*; 88th ed.; CRC Press: Boca Raton, FL, 2008.
(32) Collman, J. P.; Boulatov, R.; Sunderland, C. J.; Fu, L. *Chem. Rev.* **2004**, *104*, 561−588.
(33) Collman, J. P.; Decréau, R. A.; Lin, H.; Hosseini, A.; Yang, Y.; Dey, A.; Eberspacher, T. A. *Proc. Natl. Acad. Sci. U.S.A.* **2009**, *106*, 7320−7323.
(34) Limoges, B.; Marchal, D.; Mavré, F.; Savéant, J.-M. *J. Am. Chem. Soc.* **2006**, *128*, 2084−2092.
(35) Brittain, T.; Baker, A. R.; Butler, C. S.; Little, R. H.; Lowe, D. J.; Greenwood, C.; Watmough, N. J. *Biochem. J.* **1997**, *326*, 109−115.
(36) Ichikawa, Y.; Nakajima, H.; Watanabe, Y. *ChemBioChem* **2006**, *7*, 1582−1589.
(37) Renault, C.; Balland, V.; Martinez-Ferrero, E.; Nicole, L.; Sanchez, C.; Limoges, B. *Chem. Commun.* **2009**, 7494−7496.
(38) Andrieux, C. P.; Limoges, B.; Marchal, D.; Savéant, J.-M. *Anal. Chem.* **2006**, *78*, 3138−3143.